

# On the origin of the fast solar wind in polar coronal funnels

P. Hackenberg<sup>1</sup>, E. Marsch<sup>2</sup>, and G. Mann<sup>1</sup>

<sup>1</sup> Astrophysikalisches Institut Potsdam, An der Sternwarte 16, 14482 Potsdam, Germany

<sup>2</sup> Max-Planck-Institut für Aeronomie, Max-Planck-Strasse 2, 37191 Katlenburg-Lindau, Germany

Received 18 January 2000 / Accepted 6 June 2000

**Abstract.** Funnels are open magnetic structures connecting the chromosphere with the solar corona (Axford & McKenzie 1997; Marsch & Tu 1997; Hackenberg et al. 1999). We investigate the stationary plasma flow out of funnels with a flux-tube model. The funnel area function is derived from an analytical 2-D magnetic field model. Since the funnel height is only approximately 15 Mm, the area function for greater heights is taken from the Banaszekiewicz et al. (1998) coronal magnetic field model. Thus we obtain a realistic area function being valid into the upper corona.

The plasma in the funnel is treated with two-fluid equations including radiative losses, thermal conduction, electron-proton heat exchange, proton heating by cyclotron-damped Alfvén waves and Alfvén wave pressure. We adjust the free parameters to the quantities measured in the lower solar corona ( $\approx 100\,000$  km above the photosphere) by SUMER aboard SOHO (Wilhelm et al. 1998). The thereby obtained height profiles of the plasma properties (e.g. density, electron and proton temperatures, flow speed) within the funnel are presented and compared with recent SUMER measurements.

**Key words:** Sun: corona – Sun: solar wind – Sun: transition region

## 1. Introduction

Recent results from Hassler et al. (1999) and Wilhelm et al. (2000), who have analyzed SUMER observations of polar coronal holes, indicate that strong outflow (largely blueshifted EUV emission lines of Ne VIII) of the nascent fast solar wind occurs mainly at the boundaries of supergranular convection cells. It is well known that the magnetic field is also concentrated at these boundaries due to the plasma flow in the convection zone (e.g., Gabriel 1976 or Parker 1992). Since the plasma beta is very small (circa  $10^{-4}$  to  $10^{-2}$ ) in the transition region and the lower corona, the magnetic field there is only very slightly influenced by plasma flows. Thus we are able to determine the magnetic field in this low-beta region independently of plasma flows. We

find a diverging magnetic field, which tends (coming from its compressed state in the convection zone) to expand initially and to become finally homogeneous in the corona. The solar wind flows through this funnel structure, which is described by the magnetic field, and exactly follows the magnetic field lines.

Given a mechanical wave energy input at the bottom of the funnel, it is unavoidable to have slow outflows everywhere on open field lines. In fact, outflow is a must because we know from in situ measurements the mass flux in the wind. The mass flux is generated and replenished continuously in the upper chromospheric network. Thus there will be outflow across the whole funnel area with a varying flow speed profile at the top cross section of the funnel, since all the field lines there are open. For convenience and to keep the model simple we shall concentrate only on the central field line in the funnel. The calculation of the flow along non-central field lines will be left to a future paper.

The main goal of our investigation is, to find out in which way the solar wind evolves on its way through the funnel and what the plasma properties in the funnel are. Thereby the flow close to the surface must be in agreement with SUMER/SOHO observations in Ne VIII of up flow (blue shifts). Also the Ulysses mass flux, which puts when mapped back to the funnel bottom a constraint on the flow, and more importantly requires continuous flow must be taken into account.

Since solar wind diagnostics by spectroscopic means begins mostly at heights of 20–30 Mm above the photosphere (David et al. 1998; Tu et al. 1998; Wilhelm et al. 1998), which is well above the funnel structure ending at approximately 15 Mm, it turned out that we have to extend the model to greater heights. We decided to enlarge the model's upper boundary to the height where we reach Parker's sonic-critical point (at approximately two solar radii according to our model, which corresponds to earlier results by Hollweg (1986)). This is very close to the Sun when compared to the Parker model and also closer than most present fast solar wind models have located it. Now at the latest the outflow which is dynamically but not energetically less important well below this point becomes relevant.

The two-fluid approach used in our investigation goes beyond traditional transition region modelling, for which the classical example is the VAL atmosphere (Vernazza et al. 1981), and which is reviewed in the book by Mariska (1992). To our knowledge only Marsch & Tu (1997)

---

Send offprint requests to: G. Mann (gmann@aip.de)

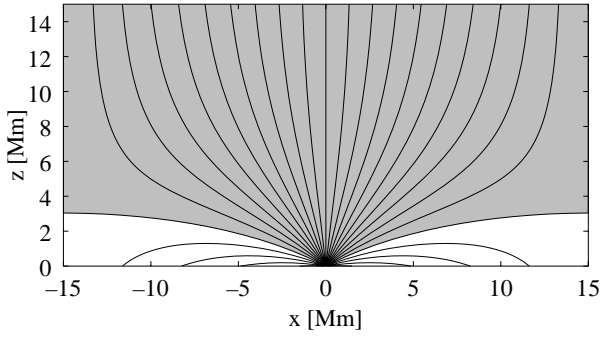


**Fig. 1.** The magnetic field above the border of two adjacent supergranules builds up the funnel structure. The region of open field lines is marked with gray color. The parameters are:  $L = 30$  Mm,  $d = 0.34$  Mm,  $B_0 = 11.8$  G,  $B_{\max} = 1.5$  kG. The photospheric level is at  $z = 0$ , and the supergranular boundaries are at  $x = 0$ .

and McKenzie et al. (1998) have described the funnel and flows in terms of separate electron and proton energy equations with wave dissipation and a common momentum equation including the wave pressure gradient force. The magnetic field modelled here on the basis of the Maxwell equations is genuine and new (but Gabriel (1976) also developed a MHD model which was the fundamental starting point for transition region models). The originality of our work is the two-fluid approach with a realistic magnetic field and in compliance with the recent SOHO observational constraints.

## 2. Magnetic field configuration

The magnetic field consists of two parts, the lower “funnel” region and the upper “coronal” region. In the lower region ( $z < 15$  Mm,  $z$  is the height above the photosphere) the global polar magnetic field is nearly constant and homogeneous at  $B_0 = B_{\text{glob}}(z=0) = 11.8$  G. At greater heights in the upper region, according to Banaszkiewicz et al. (1998), it is formed by three components, a dipole, a quadrupole and an equatorial current sheet, which together result in

$$B_{\text{glob}}(r) = M \left( \frac{2}{r^3} + \frac{3Q}{r^5} + \frac{K}{a_1(r+a_1)^2} \right) \quad (1)$$

with the distance  $r$  measured in solar radii from the center of the Sun, i.e.  $r = z/R_{\odot} + 1$ , and the constants  $M = 1.789$  G,  $Q = 1.5$ ,  $K = 1.0$  and  $a_1 = 1.538$ .

In the funnel region the magnetic field is not homogeneous, but rather very inhomogeneous, which is modelled by superposing the homogeneous field supplied by (1) with the result of a two-dimensional funnel model.

For this 2-D model we assume two adjacent supergranules (each with diameter  $L = 30$  Mm) placed symmetrically left and right of  $x = 0$  with their centers at  $x = -L/2$  and  $x = +L/2$ , see Fig. 1. To keep the model as simple as possible we further assume a very high degree of symmetry by imposing four planes of symmetry (i.e. mirrors) at  $x = -L/2$ ,  $x = 0$ ,  $x = +L/2$  and  $y = 0$ . The magnetic field can be expressed by its vector potential  $A$ , which yields in two dimensions

$$\mathbf{B} = \nabla A(x, z) \times \mathbf{e}_y. \quad (2)$$

Calculating the electric current from the magnetic field,

$$\frac{4\pi}{c} \mathbf{j} = \nabla \times \mathbf{B} = -\mathbf{e}_y \Delta A, \quad (3)$$

we note that it is perpendicular to the  $x$ - $z$  plane and thus forbidden by the imposed  $y = 0$  symmetry plane, i.e., the electric current  $\mathbf{j}$  must be zero and the vector potential  $A$  obeys the Laplace equation

$$\Delta A = 0. \quad (4)$$

That is, we have a potential magnetic field. The homogeneous “background” magnetic field  $B_0$  is separated by defining

$$A(x, z) = A_0(x, z) + B_0 x. \quad (5)$$

Then the Laplace Eq. (4) is solved with the Dirichlet boundary conditions,  $A_0 = 0$  at  $x = \pm L/2$  (due to the imposed symmetry), and  $A_0 = 0$  for  $z \rightarrow \infty$ . At the bottom, i.e. at  $z = 0$ , the compressed magnetic field is assumed to be the step function

$$B_z(x, z=0) = \begin{cases} B_{\max} & -\frac{d}{2} \leq x \leq \frac{d}{2} \\ -\frac{B_{\max}d - B_0L}{L-d} & \text{elsewhere,} \end{cases} \quad (6)$$

which is easily integrated along the  $x$  axis. This results in a sawtooth function

$$A_0(x, z=0) = (B_{\max} - B_0) \times \begin{cases} \frac{-d(L+x)}{L-d} & -\frac{L}{2} \leq x \leq -\frac{d}{2} \\ x & -\frac{d}{2} \leq x \leq \frac{d}{2} \\ \frac{d(L-x)}{L-d} & \frac{d}{2} \leq x \leq \frac{L}{2} \end{cases} \quad (7)$$

defining the boundary condition at  $z = 0$ . The solution to these boundary conditions is formally denoted by

$$A_0(x, z) = \frac{1}{L} \int_0^{\frac{L}{2}} A_0(\xi, z=0) \left( \frac{\sinh \frac{2\pi}{L} z}{\cosh \frac{2\pi}{L} z - \cos \frac{2\pi}{L}(\xi - x)} - \frac{\sinh \frac{2\pi}{L} z}{\cosh \frac{2\pi}{L} z - \cos \frac{2\pi}{L}(\xi + x)} \right) d\xi. \quad (8)$$

Note that this integral cannot be solved in a closed form with the boundary condition (7). However, it is possible to denote the magnetic field in a closed form:

$$B_x(x, z) = \frac{B_{\max} - B_0}{2\pi} \frac{L}{L-d} \ln \frac{\cosh \frac{2\pi}{L} z - \cos(\frac{\pi}{L}d + \frac{2\pi}{L}x)}{\cosh \frac{2\pi}{L} z - \cos(\frac{\pi}{L}d - \frac{2\pi}{L}x)} \quad (9)$$

$$B_z(x, z) = B_0 + (B_{\max} - B_0) \left\{ -\frac{d}{L-d} + \frac{L}{L-d} \frac{1}{\pi} \times \left( \arctan \frac{\cosh \frac{2\pi}{L} z \sin \frac{\pi}{2L}d + \sin(\frac{\pi}{2L}d + \frac{2\pi}{L}x)}{\sinh \frac{2\pi}{L} z \cos \frac{\pi}{2L}d} + \arctan \frac{\cosh \frac{2\pi}{L} z \sin \frac{\pi}{2L}d + \sin(\frac{\pi}{2L}d - \frac{2\pi}{L}x)}{\sinh \frac{2\pi}{L} z \cos \frac{\pi}{2L}d} \right) \right\}. \quad (10)$$

This analytical 2-D solution for the magnetic field is depicted in Fig. 1.

The last open field line, i.e. the boundary between the white and gray region in Fig. 1, shows a rectangular kink when it

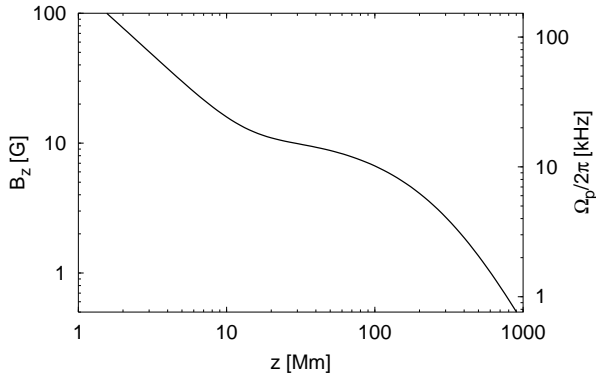


**Fig. 2.** The magnetic field at the central line of the funnel, i.e. at  $x = 0$ . On the right hand side the corresponding proton cyclotron frequency is shown.

reaches the outer wall of the box at  $x = \pm L/2$ . A closer inspection of Eqs. (9) and (10) reveals that the magnetic field vanishes there. We define the height  $h_b$  of the boundary field line there by  $B_z(x = \pm L/2, z = h_b) = 0$ , which is then given by

$$h_b = \frac{L}{\pi} \operatorname{Arctanh} \frac{\tan \frac{\pi}{2} \frac{B_{\max} d - B_0 L}{(B_{\max} - B_0) L}}{\tan \frac{\pi d}{2L}}. \quad (11)$$

In the example solution shown in Fig. 1, the parameter  $d$  has been chosen in such a manner that  $h_b \approx 3$  Mm.

On the central line of the funnel, i.e. at  $x = 0$ , the solution (9) for  $B_x$  vanishes and Eq. (10) reads (with the first  $B_0$  already substituted by  $B_{\text{glob}}$  to take the global magnetic field into account):

$$B_z(z) = B_{\text{glob}}(z) + \frac{B_{\max} - B_0}{L - d} \times \left[ L \frac{2}{\pi} \arctan \left( \coth \frac{\pi}{L} z \tan \frac{\pi d}{2L} \right) - d \right]. \quad (12)$$

This function is plotted in Fig. 2. The second term on the right-hand side of Eq. (12) becomes small for heights above 15 Mm and is negligible above 30 Mm.

As a rule of thumb it may be stated that each structure of typical length  $l$ , which is imposed on a potential magnetic field (e.g., by boundary conditions), decays on the same length scale  $l$ . This is also true for the magnetic field coming out from the photosphere on the distance  $d$ : we have tested various lengths  $d$  between 0.3 and 1 Mm (thereby adjusting  $B_{\max}$ , so that  $h_b$  is held constant at 3 Mm) and found that the magnetic field is significantly changed only within a circle of 1 Mm radius around the origin ( $x = 0, z = 0$ ). This also implies that, any errors introduced by our ad hoc defined boundary condition (6) becomes smaller with increasing height  $z$  and may be well negligible at the bottom of our funnel model at  $z_b \approx 2$  Mm.

We are aware of the fact that in the magnetically closed regions (white regions in Fig. 1) the plasma is hot and the magnetic field is weak, i.e., our low-beta assumption is not a very good one, especially near the points ( $x = \pm L/2, z = h_b$ ). The magnetic field there is inaccurate and the boundary between open and closed field lines is somewhat shifted by the thermal

pressure. At  $x = \pm L/2$  the boundary field line might even be shifted to heights of 7 or 8 Mm. But these effects becomes smaller and smaller the deeper we go into the region of open field lines (gray regions in Fig. 1) and towards the central line of the funnel. Thus our magnetic field model is adequate on the central line, from where Eq. (12) is derived.

### 3. The heating function

We assume that the plasma heating is entirely done by Alfvén waves which are dissipated by kinetic processes near the proton-cyclotron resonance. By this heating mechanism, only the protons are heated. The electrons are not directly heated, but receive heat by Coulomb collisions with the hotter protons (see Sect. 4).

The heating process due to frequency sweeping is rather general and just depends on inhomogeneity, whatever the detailed dissipation mechanism may be. It should not depend strongly on the kinetics as long as all waves crossing the cyclotron-frequency border are sent to dissipation. There is ample literature in the solar wind about this. We refer to Marsch (1999) for further discussions of this problem.

We also assume that the Alfvén waves are not generated while the plasma is traversing the funnel, but rather that the power spectrum density,  $P$ , originates below and is completely injected at the bottom of the funnel, with a spectral power law index of  $-1$ , i.e.,

$$P(\omega, z_0) = P(\omega_0, z_0) \left( \frac{\omega}{\omega_0} \right)^{-1}. \quad (13)$$

The Alfvén wave spectrum might be produced, e.g., by reconnection which causes microflares according to the Axford et al. (1999) “furnace” model or by stochastic reconnections as proposed by Ruzmaikin & Berger (1998).

The lateral dimension of the funnel is approximately 7 Mm at its bottom (at a height of  $z_b \approx 2$  Mm above the photosphere), where the transition region is situated, if we define the funnel by the region of open field lines. Because of this limited width and the high Alfvén velocity there, very-low-frequency waves cannot be generated efficiently. Therefore we assume that the wave spectrum has a lower cut-off frequency of  $\omega_L/2\pi = 1$  Hz.

At the high frequencies in the vicinity of the gyro frequency  $\Omega_p$  the energy contained in the wave spectrum is transferred to the plasma by cyclotron-resonance damping. This damping already happens at a frequency  $\omega_H$  which is somewhat below the proton-cyclotron frequency  $\Omega_p$ . In our case of a very low plasma beta we take  $\omega_H = 0.8 \Omega_p$ . In particular, we do not separately calculate the cyclotron wave dissipation caused by minor ions with a higher charge-to-mass ratio (Cranmer et al. 1999; Cranmer 2000), because in the end the minor ions – they become hotter than the protons – transfer the energy they have absorbed to the protons by Coulomb collisions. Since we assume that the dissipated part of the wave spectrum is not replenished, the total absorbed wave energy and the thermal energy the protons receive are the same. However, in the outer solar corona and the interplanetary medium (which is beyond the scope of our model) these assumptions do not longer hold and a different

approach is necessary. The simple heating function used here implies that wave energy is transferred from the spectrum directly at the frequency  $\omega_H$  to the plasma. This heating function after Tu & Marsch (1997) reads

$$H(z) = -(v + v_A) P(\omega_H, z) \frac{\partial}{\partial z} \omega_H(z) \quad (14)$$

with the Alfvén velocity  $v_A = B_z/(4\pi\rho)^{1/2}$ . This heating function is only an approximation but reflects a pivotal aspect of the physics going on in the wave dissipation process. It describes that by frequency sweeping the high-frequency part of the wave spectrum is dissipated at a rate given by the transit time of an Alfvén wave through the magnetic-field scale height, which is also the scale at which the ion gyrofrequency changes spatially. There are other processes, such as cascading, that might lead to replenishing of the spectrum. The kinetic physics of the wave-damping process in the dissipation domain is certainly much more complicated and still not understood well. For a further discussion see Marsch (1999) and references therein.

The spatial evolution of the wave energy-density spectrum  $P$  is described by a spectral transfer equation (Jacques 1977; Tu et al. 1984; Tu & Marsch 1997; Marsch 1998). We do not solve the spectral transfer equation here self-consistently, but make the simplifying assumption that the spectrum is of a rigid power-law form up to the dissipation regime, which ensures substantial wave amplitudes at the resonance frequency and implies tacitly efficient nonlinear wave energy transfer. This is a crucial assumption which implies that in the source region of the high-frequency waves injected at the bottom of the funnel local turbulence or the wave generation process itself produced a power-law spectrum. Since the background field is strong the linear WKB approximation for the wave propagation seems appropriate for waves with frequencies below the proton gyrofrequency. The work done by the wave-pressure-gradient force on the plasma flow is accounted for by the spatial variation of the wave power spectrum which in an integrated form can be written as

$$P(\omega, z) = P(\omega, z_0) \frac{M_A(z_0)(1 + M_A(z_0))^2}{M_A(z)(1 + M_A(z))^2} \quad (15)$$

depending on the Alfvén Mach number  $M_A = v/v_A$ . Since this equation has been derived by a WKB method, the wavelength must be much smaller than the geometrical spatial variation. This condition is satisfied by our chosen  $\omega_L$ . The Alfvénic wave pressure, also derived by the WKB method, reads

$$p_A = \frac{\langle b^2 \rangle}{8\pi} = \frac{1}{2} \int_{\omega_L}^{\omega_H} P(\omega) d\omega, \quad (16)$$

and the total energy flux carried by the waves is

$$F = \left(\frac{3}{2}v + v_A\right) \frac{\langle b^2 \rangle}{4\pi} = (3v + 2v_A) p_A. \quad (17)$$

The average velocity amplitude of the Alfvén waves  $\xi$  may be estimated by

$$\xi = \left(\frac{\langle b^2 \rangle}{4\pi\rho}\right)^{1/2} = \left(\frac{2p_A}{\rho}\right)^{1/2}. \quad (18)$$

In our subsequent calculations we choose  $P(\omega_0, z_0)$  in such a way that  $F$  takes a value appropriate to maintain the fast solar wind (see discussion below). Since we did not consider spectral transfer but only local dissipation the spectral slope remains invariant and stays at the value of the original spectrum (13). In the inertial range below the frequency  $\omega_H$  the spectral intensity declines spatially according to (15). In the dissipation regime above  $\omega_H$ , the power drops to zero and is not replenished thereafter, but all the wave energy is sent to dissipation, thus defining the heating function (14). Inhomogeneity, i.e., the spatial decline of  $\omega_H(z)$  is essential for the heating mechanism used here. The spatial evolution of the power spectrum is illustrated in the paper by Tu & Marsch (1997). With increasing height an ever larger part of the original high-frequency wave power given by (13) ends up irreversibly in thermal proton energy.

#### 4. Model equations

In this section we describe the equations governing the plasma flow through the funnel structure. Since the magnetic field is already known, we make a thin flux-tube approximation. Magnetic flux conservation yields for the virtual flux tube the cross-section area  $A$  (not to be confused with the magnetic vector potential in Sect. 2, which is only used there)

$$A(z) = \frac{A_0 B_0}{B_z(z)}. \quad (19)$$

We further assume that the plasma flow is in steady state, i.e., we average in time over all transient fluctuations/disturbances and only consider mean values. Thus the total mass flux  $\dot{M} = \Phi_m A = \Phi_{m0} A_0$  in the virtual tube is conserved, yielding the speed

$$v = \frac{\dot{M}}{\rho A} = \frac{\Phi_{m0} A_0}{\rho A}. \quad (20)$$

The estimated mass flux at the Sun's surface (more precisely: at the upper end of the funnel where  $B_z = B_0$ , i.e., at  $z \approx 16$  Mm) is taken to be  $\Phi_{m0} = 1.5 \cdot 10^{-10}$  g/(cm<sup>2</sup> s). This corresponds to a proton flux of  $2.0 \cdot 10^8$ /(cm<sup>2</sup> s) at 1 AU (Barnes et al. 1995) increased by the extra-spherical expansion factor of 10.2, resulting from the Banaszekiewicz et al. (1998) magnetic-field model.

Quasineutrality and the electric-current-free state of the plasma lead to equal density and velocity of electrons and protons, i.e.,  $n = n_e = n_p$  and  $v = v_e = v_p$ . The momentum equation with the partial thermal pressures

$$p_e = nk_B T_e, \quad p_p = nk_B T_p, \quad (21)$$

the Alfvén wave pressure  $p_A$  and the gravitational acceleration  $g = GM_\odot/(z + R_\odot)^2$  reads

$$\rho v \frac{\partial}{\partial z} v = -\frac{\partial}{\partial z} (p_e + p_p + p_A) - \rho g. \quad (22)$$

The energy equation for electrons ( $\alpha = e$ ) and protons ( $\alpha = p$ ),

$$\frac{vnk_B}{\gamma-1} \frac{\partial}{\partial z} T_\alpha + \frac{nk_B T_\alpha}{A} \frac{\partial}{\partial z} Av = \mathcal{S}_\alpha, \quad (23)$$

**Table 1.** The radiative loss function of an optically thin plasma, adapted from Rosner et al. (1978).

$P_r(T_e)$ [erg cm <sup>3</sup> /s]	$T_e$ [K]
$1.41 \cdot 10^{-22}$	20 000– 37 550
$1.00 \cdot 10^{-31} T_e^2$	37 550– 79 436
$6.31 \cdot 10^{-22}$	79 436– 251 146
$3.98 \cdot 10^{-11} T_e^{-2}$	251 146– 562 025
$1.26 \cdot 10^{-11}$	562 025– 1 999 812
$2.00 \cdot 10^{-11} T_e^{-2/3}$	1 999 812–10 000 000

contains an (external) energy source term  $\mathcal{S}_\alpha$ . This term, which reads

$$\mathcal{S}_e = -L_r - \nabla \cdot \mathbf{q}_e + Q_{ep} \quad (24)$$

for the electrons and

$$\mathcal{S}_p = H - \nabla \cdot \mathbf{q}_p - Q_{ep} \quad (25)$$

for the protons, takes care of the various energy sources and losses of the plasma, which are subsequently given ( $H$  has been already discussed).

The energy removed locally (or deposited, if negative) by thermal conduction due to electrons ( $\alpha = e$ ) and protons ( $\alpha = p$ ) is

$$\nabla \cdot \mathbf{q}_\alpha = -\frac{1}{A} \frac{\partial}{\partial z} \left( A \kappa_\alpha \frac{\partial}{\partial z} T_\alpha \right). \quad (26)$$

From the numbers and formulas given by Hinton (1983), one obtains (assuming a Coulomb logarithm of  $\ln \Lambda = 18$ )

$$\kappa_e = \kappa_0 T_{ep}^{3/2} T_e \quad \text{and} \quad \kappa_p = \frac{\kappa_0}{24.8} T_p^{5/2} \quad (27)$$

with  $\kappa_0 = 1.02 \cdot 10^{-6}$  erg/(cm s K<sup>7/2</sup>) and with the weighted mean electron-proton temperature  $T_{ep} = (m_p T_e + m_e T_p)/(m_e + m_p)$ . The electron-proton heat-exchange term is also given by Hinton (1983) and reads

$$Q_{ep} = \frac{(32\pi m_e m_p)^{1/2} n^2 e^4 (\ln \Lambda) k_B (T_p - T_e)}{(m_e + m_p)^{3/2} (k_B T_{ep})^{3/2}}, \quad (28)$$

which in short is

$$Q_{ep} = Q_0 n^2 T_{ep}^{-3/2} (T_p - T_e) \quad (29)$$

with  $Q_0 = 1.47 \cdot 10^{-17}$  erg cm<sup>3</sup> K<sup>1/2</sup>/s.

The electrons give, by collisional line excitations, thermal energy to photons. The resulting radiative losses are calculated using

$$L_r = n^2 P_r(T_e). \quad (30)$$

Suitable values for the radiative loss function  $P_r$  are given in Table 1.

Finally, we obtain a set of ordinary differential equations (ODEs) of order five

$$\rho' = \frac{\rho}{A} \frac{\dot{M}^2 A' + A^2 \rho^2 \frac{k_B}{m} (q_e/\kappa_e + q_p/\kappa_p) - A^3 \rho^2 \tilde{g}}{A^2 \rho p_{\text{eff}} - \dot{M}^2} \quad (31)$$

**Table 2.** Typical plasma parameters in interplume lanes determined by Wilhelm et al. (1998) from SUMER measurements.

$z$ [Mm]	$n_e$ [cm <sup>-3</sup> ]	$T_e$ [K]
21	$8.2 \cdot 10^7$	$7.8 \cdot 10^5$
35	$7.1 \cdot 10^7$	$8.1 \cdot 10^5$
56	$5.2 \cdot 10^7$	$8.1 \cdot 10^5$
118	$2.2 \cdot 10^7$	$8.7 \cdot 10^5$
209	$7.6 \cdot 10^6$	$8.8 \cdot 10^5$

$$T_e' = -\frac{q_e}{\kappa_e A} \quad (32)$$

$$T_p' = -\frac{q_p}{\kappa_p A} \quad (33)$$

$$q_e' = -A(L_{re} + Q_{ep}) + \frac{\dot{M} k_B}{m} \left[ \frac{T_e \rho'}{\rho} - \frac{T_e'}{\gamma-1} \right] \quad (34)$$

$$q_p' = A(H_p + Q_{ep}) + \frac{\dot{M} k_B}{m} \left[ \frac{T_p \rho'}{\rho} - \frac{T_p'}{\gamma-1} \right] \quad (35)$$

with, taking the Alfvén wave pressure  $p_A$  into account, an effective pressure

$$p_{\text{eff}} = n k_B (T_e + T_p) + \frac{1 + 4M_A + 3M_A^2}{2 + 4M_A + 2M_A^2} p_A \quad (36)$$

and a modified gravitational acceleration

$$\tilde{g} = g - \frac{p_A}{\rho \frac{\omega_H}{\omega_L} \ln \frac{\omega_H}{\omega_L}} \frac{\partial}{\partial z} \omega_H. \quad (37)$$

These ODEs (31)–(35) are integrated by a fifth-order Runge-Kutta method with adaptive stepsize control (Press et al. 1992).

We start the integration at  $z = 100$  Mm with  $n = 2.7 \cdot 10^7/\text{cm}^3$  and  $T_e = 0.84$  MK. These values meet the results of Wilhelm et al. (1998), which are shown in Table 2.

To maintain a fast solar wind with an asymptotic velocity of  $v_\infty = 750$  km s<sup>-1</sup> (Barnes et al. 1995) a total energy flux input,  $F_{\text{tot}} = (\frac{1}{2} v_g^2 + \frac{1}{2} v_\infty^2) \Phi_m = 3.8 \cdot 10^{15}$  erg/(cm<sup>2</sup> s), is necessary at a height of 100 Mm ( $v_g = 576$  km s<sup>-1</sup> is the escape velocity and the flux tube area ratio is  $A/A_0 = 1.77$  at this height). This corresponds to an Alfvén wave pressure  $p_A = 6.7 \cdot 10^{-4}$  dyn/cm<sup>2</sup> and to a heating rate  $H = 2.2 \cdot 10^{-6}$  erg/(cm<sup>3</sup> s), if the wave spectrum's lower boundary remains at  $\omega_L$ . But farther away from the Sun, since then also the larger structures contribute to the spectrum (e.g. magnetic network oscillations),  $\omega_L$  becomes smaller there. Thus the above calculated heating rate imposes an upper limit to the actual heating rate at 100 Mm (see also Fig. 5).

The integration is carried out in both directions, downwards and upwards. At the bottom of the funnel, i.e. downwards, we impose the boundary condition  $T_e = T_p = 40\,000$  K. This also defines the position  $z_b$  of the funnel bottom, where the transition region is situated. We do not address the ionizations of hydrogen in the first ionization layer (McKenzie et al. 1998; Peter & Marsch 1998), which is located on top of the chromosphere. In the upward direction we aim at going with the solution through Parker's sonic-critical point, i.e., both the denominator

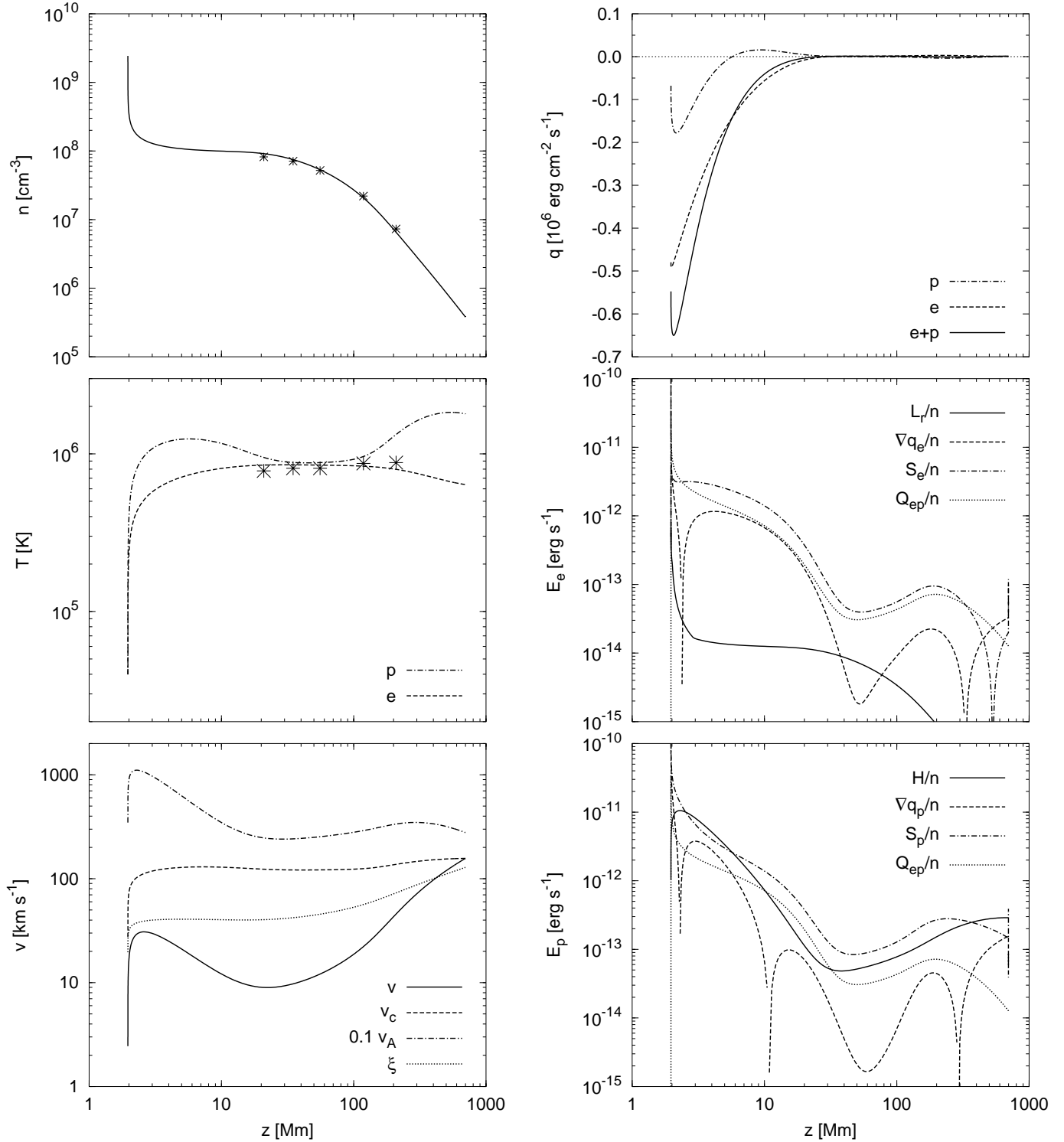


**Fig. 3.** Numerical solution of the fast solar wind evolution from the transition region to Parker’s sonic-critical point. The asterisks in the two topmost panels on the left side denote electron density and electron temperature derived by Wilhelm et al. (1998) from SUMER measurements (see Table 2).

and the numerator of the “critical” Eq. (31) have to become zero simultaneously. The denominator is zero when the plasma flow speed  $v$  equals the critical velocity  $v_c = (p_{\text{eff}}/\rho)^{1/2}$ . These boundary conditions provide two additional constraints which

determine two of the three remaining ( $n$  and  $T_e$  are already given) initial values of the ODEs.

For now let’s assume that we have a good value for  $T_p$  at  $z = 100$  Mm. Then the two other (yet unknown) initial values  $q_e$  and

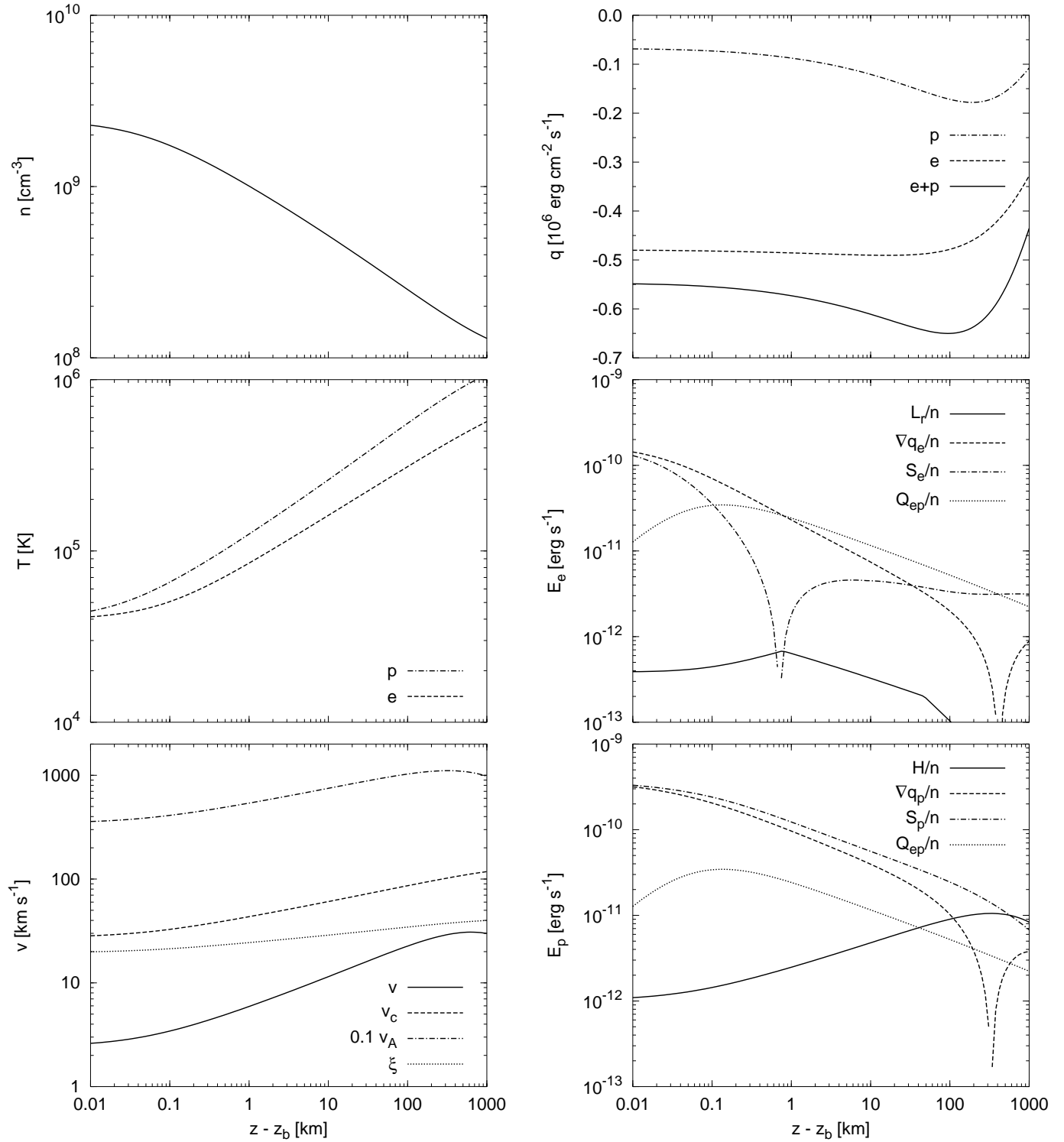


**Fig. 4.** Numerical solution of the fast solar wind evolution at the transition region. The plots shown here are an enlargement of Fig. 3 with  $z_b = 1.963$  Mm. Please note the logarithmic scale on the abscissa.

$q_p$  can be determined by a shooting method (Press et al. 1992): Some arbitrary, but reasonable values are supplied for  $q_e$  and  $q_p$  and the integration is carried out in both (upward and downward) directions. Of course, the demanded boundary conditions will not be met, they are missed by a certain amount  $\Delta(q_e, q_p)$ . All

we have to do is to minimize  $|\Delta|$  by varying  $q_e$  and  $q_p$ . The final solution for a given  $T_p$  is found when the boundary conditions are met.

It turned out that only for a certain regime in  $T_p$  we are able to find solutions conforming to the boundary conditions.

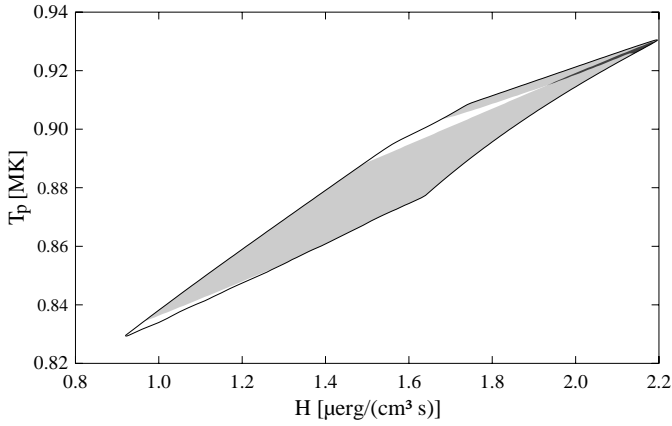


**Fig. 5.** Proton temperature and heating rate at  $z = 100$  Mm. In the confined region solutions conforming with the imposed boundary conditions do exist. The different shades of gray are explained in the text.

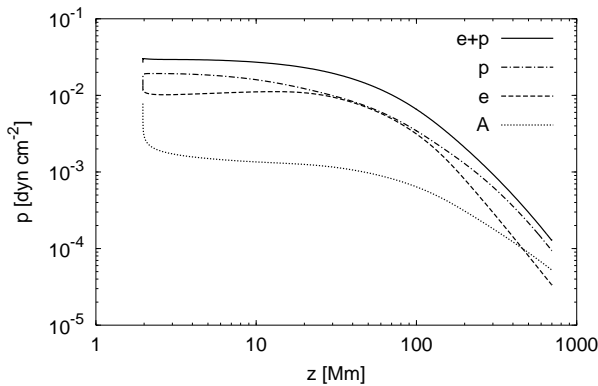


**Fig. 6.** Partial pressure in the plasma, originating from electrons (e), protons (p), and Alfvén waves (A). Also the sum of electron and proton pressure (e+p) is displayed.

To investigate this further we varied also (besides  $T_p$ ) the amplitude of the power-spectrum density  $P(\omega_0, z_0)$ , or rather the heating rate  $H$  at 100 Mm, because for this parameter we do know only an upper limit from earlier considerations. Note that due to Eqs. (13)–(15)  $P(\omega_0, z_0)$  and  $H$  are interconvertible at  $z = 100$  Mm. Within the confined region shown in Fig. 5 we have been able to find solutions satisfying the boundary conditions. However, not all of these solutions fit the measured data well (see Table 2). In the lower shaded region the calculated electron temperature does not deviate by more than 10% from the measured data. In the upper shaded region the same is true for the electron number density. The small darker shaded region in the upper right corner indicates the overlap of the two shaded regions.

As it can be seen in Fig. 5, the heating rate  $H$  at 100 Mm must be somewhat below  $2.2 \cdot 10^{-6}$  erg/(cm<sup>3</sup> s). But not too much. Otherwise the measured data are not fitted well. Therefore, for the subsequent presentation of our numerical example solution, we choose  $H = 2.1 \cdot 10^{-6}$  erg/(cm<sup>3</sup> s). At  $T_p = 0.924$  MK, the data are fitted best, given this heating rate. All initial values of the ODEs are now fixed.

## 5. Discussion

A numerical example solution of the model equations described in Sect. 4 is shown in Fig. 3. The details of the transition region are depicted in Fig. 4, which is an enlargement of the lower part of Fig. 3. Note the distortion in both pictures caused by the logarithmic scale applied to the  $z$  axis.

Both, the electron and proton temperature rises from 0.04 MK to a few 0.1 MK in a very thin region of only 20 km in height. Since the pressure there is approximately constant (the barometric pressure scale height is much larger than 20 km, cf. also Fig. 6), the density  $n$  is inversely correlated with the temperature and falls by a factor of 5.6 in the same small region. The flow speed  $v$  is correlated with the density  $n$  by Eq. (20) and therefore shows also a strong increase in this region. This increase in flow speed is not large enough to disturb the barometric scale height in a serious manner. Therefore the above-stated constant-pressure approximation still holds.

But why do we have this very steep temperature gradient at the bottom of our funnel model? The answer is given by Eqs. (27), (32), (33) and the fact that there is a large downward thermal energy flux  $q_\alpha$ , which is more or less constant (cf. Fig. 4; a factor of two does not matter) in the region of interest: The thermal conductivity  $\kappa_\alpha$  scales proportional to  $T_\alpha^{5/2}$ . When coming from high temperatures and going downwards, the temperature gradient must increase more and more to maintain the same energy flux. This makes the temperature drop even faster.

Because of the large magnetic-field gradient and the resulting large gradient in the proton cyclotron frequency, the heating function is strongest below 20 Mm. There the Coulomb collision term,  $Q_{ep}$ , is forced to transfer a lot of energy from the protons to the electrons, but does not suffice to establish temperature equilibrium. Thus a big temperature difference between the protons and electrons can arise. Above 20 Mm the heating function is much weaker, but the Coulomb collisions have still the same efficiency ( $n$  has not dropped significantly). This leads to a temperature coupling of protons and electrons, i.e., proton and electron temperature become similar. But above 100 Mm the density  $n$  drops rapidly, and then temperature coupling becomes ineffective. The proton temperature rises again.

The energy flux due to heat conduction is shown in the upper-right panel of Figs. 3 and 4. The electron heat flux (e), the proton heat flux (p) and the total heat flux (e+p) are shown. Because of the much higher proton temperatures and the steeper proton temperature gradient in the transition region at  $z \approx 2$  Mm, the proton energy flux is not much smaller than the electron heat flux, despite the factor of 24.8 in Eq. (27).

The local electron and proton energy balance per particle is shown in the two lower-right panels of Figs. 3 and 4. In both panels the modulus of the displayed quantity is plotted on a logarithmic scale. Whenever one of these quantities crosses through zero, a kink (and a small gap) in the plot arises. Note also that at Parker's sonic-critical point (at 698 Mm), where the calculation ends, only the five main variables of the ODEs are continuous. But derivatives of these variables may be and in fact are discontinuous, as it is the case with  $\nabla \cdot \mathbf{q}_\alpha$  and  $S_\alpha$ .

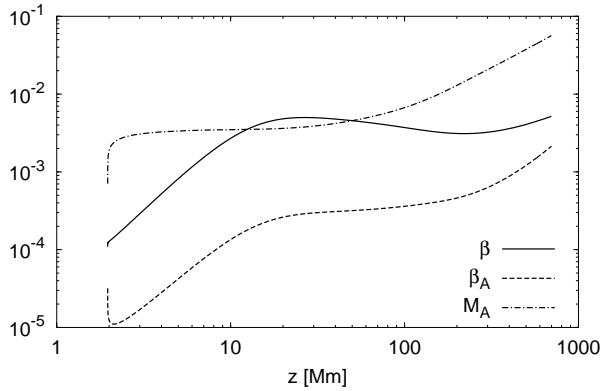


**Fig. 7.** Plasma beta ( $\beta = 8\pi(p_e + p_p)/B_z^2$ ), Alfvén wave beta ( $\beta_A = 8\pi p_A/B_z^2$ ) and Alfvén Mach number  $M_A$  versus height from the transition region to the lower solar corona.

According to the boundary condition,  $T_e = T_p$  at the funnel bottom, the electron-proton heat exchange term  $Q_{ep}$  vanishes there. This feature is clearly visible in Fig. 3, but missing in Fig. 4, because it happens within the lowest 10 m of the calculation, which are not shown in Fig. 4. Extrapolating  $Q_{ep}/n$  to  $z = z_b$  yields approximately  $10^{-10}$  erg s $^{-1}$ , which corresponds to  $T_p - T_e \approx 24\,000$  K or to  $T_p \approx 64\,000$  K and  $T_e \approx 40\,000$  K. That fact makes the originally imposed boundary condition questionable. However, some 100 m higher the influence of that boundary condition has disappeared, which makes the artificially introduced disturbance in the energy budget negligibly small, and thus this issue may well be regarded as marginal.

The plasma beta (see Fig. 7) is very small in the whole region, which proves our assumption to be correct that the magnetic field can be determined independently from the plasma, which behaves like strongly magnetized test particles in a potential field.

## 6. Conclusions

The origin of the fast solar wind in coronal funnels has been discussed in terms of a two-fluid model. Since the plasma beta is small in the height range considered, the magnetic field can be calculated as potential field. It has been shown that sub-Alfvénic outflow can be driven by thermal pressure-gradient forces maintained by high-frequency wave-energy absorption. Only the protons are heated by ion-cyclotron wave dissipation, whereas the electrons lose thermal energy through radiative losses. The average wave amplitudes  $\xi$  required are compatible with observational values inferred from SOHO for spectral line turbulent broadenings. The energy flux is consistent with the in-situ requirements (obtained from 1 AU plasma measurements) for fast solar wind streams.

For both species classical heat conduction is considered in the funnel. The downward conduction of heat from the hot corona leads to a very steep temperature gradient, a temperature discontinuity, simultaneously for both species. These steep temperature rises occur independently of the details of the heat-

ing function and funnel geometry, which both have an intrinsic scale height in proportion to that of the magnetic field (of the order of Mm) and also arises in static atmospheres. This discontinuity in both the electron and proton temperature (which has also been found by Marsch & Tu (1997)) is a new result coming from two-fluid modelling, although the thermodynamics of electrons and ions is different.

The conditions found at the top of the funnel (circa 15 Mm above the photosphere) may be used to define the bottom of a coronal hole and the boundary conditions for conventional solar wind models, usually starting from a million degree corona.

*Acknowledgements.* The authors thank the DLR (Deutsches Zentrum für Luft- und Raumfahrt) for supporting this work under Grant 50 OC 9702.

## References

- Axford W.I., McKenzie J.F., 1997, In: Jokipii J.R., Sonett C.P., Giampapa M.S. (eds.) *Cosmic Winds and the Heliosphere*. Univ. Arizona Press, p. 31
- Axford W.I., McKenzie J.F., Sukhorukova G.V., et al., 1999, *Space Sci. Rev.* 87, in press
- Banaszkiewicz M., Axford W.I., McKenzie J.F., 1998, *A&A* 337, 940
- Barnes A., Gazis P.R., Phillips J.L., 1995, *Geophys. Res. Lett.* 22, 3309
- Cranmer S.R., 2000, *ApJ* 532, 1197
- Cranmer S.R., Field G.B., Kohl J.L., 1999, *ApJ* 518, 937
- David C., Gabriel A.H., Bely-Dubau F., et al., 1998, *A&A* 336, L90
- Gabriel A.H., 1976, *Phil. Trans. R. Soc. London* 281, 339
- Hackenberg P., Mann G., Marsch E., 1999, *Space Sci. Rev.* 87, 207
- Hassler D.M., Dammasch I.E., Lemaire P., et al., 1999, *Sci* 283, 810
- Hinton F.L., 1983, In: Galeev A.A., Sudan R.N. (eds.) *Basic Plasma Physics I*, Vol. 1 of *Handbook of Plasma Physics*, North-Holland Pub., p. 147
- Hollweg J.V., 1986, *J. Geophys. Res.* 91, 4111
- Jacques S.A., 1977, *ApJ* 215, 942
- Mariska J.T., 1992, *The Solar Transition Region*. Vol. 23 of *Cambridge Astrophysics Series*, Cambridge University Press, Cambridge
- Marsch E., 1998, In: Vial J.C., Bocchialini K., Boumier P. (eds.), *Space Solar Physics: Theoretical and Observational Issues in the Context of the SOHO Mission*. Vol. 507 of *Lecture Notes in Physics*, Orsay (France) 1–13 Sept. 1997, Springer, p. 107
- Marsch E., 1999, *Nonlin. Proc. Geophys.* 6, 149
- Marsch E., Tu C.-Y., 1997, *Sol. Phys.* 176, 87
- McKenzie J.F., Sukhorukova G.V., Axford W.I., 1998, *A&A* 330, 1145
- Parker E.N., 1992, *J. Geophys. Res.* 97, 4311
- Peter H., Marsch E., 1998, *A&A* 333, 1069
- Press W.H., Teukolsky S.A., Vetterling W.T., Flannery B.P., 1992, *Numerical recipes in Fortran: the art of scientific computing*. Cambridge University Press, Cambridge
- Rosner R., Tucker W.H., Vaiana G.S., 1978, *ApJ* 220, 643
- Ruzmaikin A., Berger M.A., 1998, *A&A* 337, L9
- Tu C.-Y., Marsch E., 1997, *Sol. Phys.* 171, 363
- Tu C.-Y., Marsch E., Wilhelm K., Curdt W., 1998, *ApJ* 503, 475
- Tu C.-Y., Pu Z.-Y., Wei F.-S., 1984, *J. Geophys. Res.* 89, 9695
- Vernazza J.E., Avrett E.H., Loeser R., 1981, *ApJS* 45, 635
- Wilhelm K., Dammasch I.E., Marsch E., Hassler D.M., 2000, *A&A* 355, 749
- Wilhelm K., Marsch E., Dwivedi B.N., et al., 1998, *ApJ* 500, 1023